

# Potassium-Containing $\alpha$ -MnO<sub>2</sub> Nanotubes: The Impact of Hollow Regions on Electrochemistry

To cite this article: Jianping Huang et al 2021 J. Electrochem. Soc. 168 090559

#### Manuscript version: Accepted Manuscript

Accepted Manuscript is "the version of the article accepted for publication including all changes made as a result of the peer review process, and which may also include the addition to the article by IOP Publishing of a header, an article ID, a cover sheet and/or an 'Accepted Manuscript' watermark, but excluding any other editing, typesetting or other changes made by IOP Publishing and/or its licensors"

This Accepted Manuscript is ©.

During the embargo period (the 12 month period from the publication of the Version of Record of this article), the Accepted Manuscript is fully protected by copyright and cannot be reused or reposted elsewhere.

As the Version of Record of this article is going to be / has been published on a subscription basis, this Accepted Manuscript will be available for reuse under a CC BY-NC-ND 3.0 licence after the 12 month embargo period.

After the embargo period, everyone is permitted to use copy and redistribute this article for non-commercial purposes only, provided that they adhere to all the terms of the licence <a href="https://creativecommons.org/licences/by-nc-nd/3.0">https://creativecommons.org/licences/by-nc-nd/3.0</a>

Although reasonable endeavours have been taken to obtain all necessary permissions from third parties to include their copyrighted content within this article, their full citation and copyright line may not be present in this Accepted Manuscript version. Before using any content from this article, please refer to the Version of Record on IOPscience once published for full citation and copyright details, as permissions may be required. All third party content is fully copyright protected, unless specifically stated otherwise in the figure caption in the Version of Record.

View the article online for updates and enhancements.

## Potassium-Containing a-MnO2 Nanotubes: The Impact of Hollow Regions on Electrochemistry

Journal:	Journal of The Electrochemical Society
Manuscript ID	JES-105319.R1
Manuscript Type:	Research Paper
Date Submitted by the Author:	04-Sep-2021
Complete List of Authors:	Huang, Jianping; Stony Brook University Yan, Shan; Brookhaven National Laboratory Wu, Daren; Stony Brook University, Materials Science and Chemical Engineering Housel, Lisa; Brookhaven National Laboratory Hu, Xiaobing; Brookhaven National Laboratory Hwang, Sooyeon; Brookhaven National Laboratory Wang, Lei; Brookhaven National Laboratory, Energy and Photon Sciences Directorate Tong, Xiao; Brookhaven National Laboratory, Center for Functional Nanomaterials Wu, Lijun; Brookhaven National Laboratory, Condensed Matter Physics and Materials Science Zhu, Yimei; Brookhaven National Laboratory, Condensed Matter Physics and Materials Science Department Marschilok, Amy; Stony Brook University, ; Brookhaven National Laboratory, Takeuchi, Esther; Stony Brook University,
Keywords:	battery, Batteries - Lithium, manganese oxide, ion diffusion, in situ electrochemistry
Keywords:	

SCHOLARONE™ Manuscripts

### Potassium-Containing $\alpha$ -MnO<sub>2</sub> Nanotubes: The Impact of Hollow Regions on Electrochemistry

Jianping Huang, <sup>1,=</sup> Shan Yan, <sup>2,3,=</sup> Daren Wu, <sup>3,4</sup> Lisa Housel, <sup>2,3</sup> Xiaobing Hu, <sup>5</sup> Sooyeon Hwang, <sup>6</sup> Lei Wang, <sup>2,3,\*</sup> Xiao Tong, <sup>6</sup> Lijun Wu, <sup>4</sup> Yimei Zhu, <sup>4,7</sup> Amy C. Marschilok, <sup>1,2,3,4,\*</sup> Esther S. Takeuchi, <sup>1,2,3,4,\*\*</sup> and Kenneth J. Takeuchi, <sup>1,2,3,4,z</sup>

<sup>1</sup>Department of Chemistry, Stony Brook University, Stony Brook, New York 11794, USA <sup>2</sup>Interdisciplinary Science Department, Brookhaven National Laboratory, Upton, New York 11973, USA

<sup>3</sup>Institute for Electrochemically Stored Energy, Stony Brook University, Stony Brook, NY 11794 <sup>4</sup>Department of Materials Science and Chemical Engineering, Stony Brook University, Stony Brook, New York 11794, USA

<sup>5</sup>Condensed Matter Physics and Materials Science Department, Brookhaven National Laboratory, Upton, New York 11973, USA

<sup>6</sup>Center for Functional Nanomaterials, Brookhaven National Laboratory, Upton, New York 11973, USA

<sup>7</sup>Department of Physics and Astronomy, Stony Brook University, Stony Brook, New York 11794, USA

- =These authors contributed equally to this work.
- \*Electrochemical Society Member.
- \*\*Electrochemical Society Fellow
- <sup>z</sup>E-mail: kenneth.takeuchi.1@stonybrook.edu

#### **Abstract**

α-MnO<sub>2</sub> type materials have been studied as electrode materials in rechargeable batteries and electrocatalysts due to their 2×2 tunneled crystal structures capable of accommodating cations and their tunable physiochemical properties. In this study, we deliberately synthesized K<sup>+</sup> containing α-MnO<sub>2</sub> (K<sub>0.9</sub>Mn<sub>8</sub>O<sub>16</sub>) hollow nanotubes varying the dimensions of the hollow regions and level of surface defects. The K<sub>0.9</sub>Mn<sub>8</sub>O<sub>16</sub> nanotube material samples have similar crystallinity, thermal stability, and average Mn oxidation state. Oxygen surface defects in the hollow regions were revealed through detailed studies using electron energy loss spectroscopy. The impact of the hollow regions and associated surface defects on the electrochemistry of K<sub>x</sub>Mn<sub>8</sub>O<sub>16</sub> were investigated using cyclic voltammetry, galvanostatic intermittent titration technique, and galvanostatic cycling. The K<sub>0.9</sub>Mn<sub>8</sub>O<sub>16</sub> nanotubes with a large hollow region (~30 nm) and higher level of surface defects show higher apparent lithium ion diffusion coefficients and lower polarization compared to the nanotubes with a small hollow region (~10 nm). In-situ lithiation demonstrated that the dimensions of the nanotube walls expanded, but the hollow region did not change in size as result of lithiation. This research demonstrates that tuning particle architecture and surface defects can positively impact functional behavior of electrochemical storage materials.

#### Introduction

Mn-based materials have been considered as potential cathode materials for rechargeable Li/Na/Zn based batteries due to their low cost, high earth abundance, high oxidation state, and environmental friendliness. <sup>1-5</sup> Multiple polymorphs of MnO<sub>2</sub> (*i.e.*  $\alpha$ ,  $\beta$ ,  $\delta$ ,  $\lambda$ ) have been demonstrated as host materials for mono- or di-valent cations. Notably,  $\alpha$ -MnO<sub>2</sub> is a polymorph of particular interest due to its large 2×2 tunnels (4.6×4.6 Å) formed by edge- and corner-sharing MnO<sub>6</sub> octahedra. <sup>6</sup> The center of these tunnels is often occupied by a stabilizing cation (*i.e.* K<sup>+</sup>, Ag<sup>+</sup>), where the ion stabilized  $\alpha$ -MnO<sub>2</sub> materials have been studied in several battery systems due to their rigid structural framework. <sup>7-16</sup>

Various MnO<sub>2</sub> nanostructures have been investigated to improve battery function, such as nanorods<sup>16</sup>, nanotubes<sup>17</sup>, nanowires<sup>18</sup>, nanosheets<sup>19</sup>, porous spheres<sup>20</sup>, and urchin-like forms.<sup>21</sup> Among them, hollow nanostructures are an attractive morphology showing high surface area and short pathways to promote rapid ion transfer facilitating the electrochemical activity of MnO<sub>2</sub>. For example, α-MnO<sub>2</sub> hollow urchins used as cathode materials in Li ion batteries delivered improved function compared to solid urchins and dispersed nanorods.<sup>22</sup> Hollow MnO<sub>2</sub> nanospheres used for aqueous Zn-MnO<sub>2</sub> batteries achieved high specific capacity due to their unique structural properties enabling insertion of zinc ions.<sup>23</sup> Further, the use of hollow MnO<sub>2</sub> spheres effectively restrained the volume change of S<sub>8</sub> and dissolution of polysulfides during the charge-discharge processes in lithium/sulfur batteries.<sup>24,25</sup> A 3D hollow α-MnO<sub>2</sub> framework has also proved to be an efficient electrocatalyst for lithium oxygen batteries.<sup>26</sup>

In addition to the rational design of nanostructures, material defects both in the bulk and at the surface have been shown to facilitate lithium ion diffusion. For example, it has been demonstrated that Ag<sub>1.6</sub>Mn<sub>8</sub>O<sub>15.6</sub> with a low level of surface defects delivered a lower discharge capacity in lithium batteries compared to Ag<sub>1.2</sub>Mn<sub>8</sub>O<sub>14.8</sub> with a high level of defects (23 vs. 160 mAh/g).<sup>27</sup> Surface defects of the pristine/lithiated Ag<sup>+</sup>-α-MnO<sub>2</sub> were characterized and the presence of intrinsic oxygen vacancies near the surface were noted to modify the local atomic structure and valence state. This surface reconstruction resulting from oxygen vacancies can significantly affect the diffusion pathways in what are otherwise one-dimensional (1D) tunneled structures<sup>28</sup> as found in Ag<sub>1.22</sub>Mn<sub>8</sub>O<sub>16-x</sub> and Ag<sub>1.66</sub>Mn<sub>8</sub>O<sub>16-y</sub> nanorods with higher and lower vacancies, respectively. In fact, α-MnO<sub>2</sub> type materials have shown lateral lithium ion transport across one nanorod to another nanorod where the observed inter-particle transport may be associated with the surface defects of the α-MnO<sub>2</sub> nanorods. <sup>27,29-31</sup> It has also been found that sodium ions favorably diffuse through regions where oxygen vacancies are concentrated, and the samples with fewer oxygen vacancies show more significant structural deformation and more inhomogeneous sodiation.<sup>32</sup> Thus, surface defects may improve ion storage by creating additional active sites for ion insertion.

In this study, K<sub>x</sub>Mn<sub>8</sub>O<sub>16</sub> nanotubes with similar bulk material properties but different hollow region sizes, and nanotubes with similar hollow region size with different surface defects regions were prepared through control of reaction conditions during the synthesis. The bulk material properties were characterized using X-ray diffraction, X-ray absorption spectroscopy, and thermogravimetric analysis. The hollow nanotubes were studied in detail by transmission electron microscopy, the material surfaces were characterized by electron energy loss spectroscopy and X-ray photoelectron spectroscopy. In-situ lithiation within a transmission electron microscope revealed the local changes in dimension as lithiation progressed along the nanotube. This study correlates the particle architecture and surface defects of the hollow

structures with the Li based electrochemistry and provides a possible mechanism to rationalize the observed behavior.

#### Methods

**Synthesis and Characterization.** K<sub>x</sub>Mn<sub>8</sub>O<sub>16</sub> samples were synthesized using a hydrothermal method as previously described.<sup>33</sup> Briefly, potassium permanganate (KMnO<sub>4</sub>) and concentrated HCl were added in deionized water. The reactions were performed at 140°C for 3, 12, and 36 h, respectively in PTFE lined autoclaves. The precipitates were washed with deionized water, dried, and annealed at 300°C for 2 h.

Synchrotron-based XRD was performed at NSLS-II, Brookhaven National Laboratory. The beam was calibrated to a wavelength of 0.1825 Å, and the samples were sealed in polyimide capillary tubes for measurements. GSAS II was utilized to perform Rietveld refinement.<sup>34</sup>

Thermogravimetric analysis (TGA) of as-prepared samples was conducted using a TA instruments SDT Q600 under nitrogen gas. The K/Mn ratio was determined by inductively coupled plasma-optical emission spectroscopy (ICP-OES) measurements using a Thermo Scientific iCAP 6300 series spectrometer.

High-angle-annular-dark-filed (HAADF) images and associated electron energy loss spectrum (EELS) analyses were acquired using the probe corrected ARM 200CF (JEOL Ltd.) which was equipped with a cold-field emission gun and GIF Quantum (Gatan, Inc.) with dual EELS system and operated at 200 kV. The EELS data was collected in scanning transmission electron microscopy (STEM) mode. The used convergence and collection semi-angle for EELS analyses are 40 mrad and 90 mrad respectively. The highest accessible energy resolution was around 0.45 eV, as determined from the full-width at half-maximum of the zero-loss peak. All background signals in the EELS profiles were subtracted using a power law fitting method. The energy positions of Mn- $L_{2,3}$  were determined by fitting the EELS profile with a combined Gaussian and Lorentz function. The white line ratio of  $L_3/L_2$  was calculated using the Pearson method with double step functions<sup>35</sup>.

X-ray photoelectron spectroscopy (XPS) was conducted using a UHV chamber equipped with the SPECS Phoibos HSA3500 analyzer and an X-ray source (hv = 1253.6 eV) operating with an accelerating voltage of 13 kV and a current of 15 mA located at the Center for Functional Nanomaterials at Brookhaven National Laboratory. All spectra were calibrated using the binding energy of C 1s peak at 284.8 eV. The CasaXPS software was used to fit the XPS spectra, and the built-in Monte Carlo approach was used to estimate the errors of fitting parameters.

Scanning electron microscopy (SEM) images and energy dispersive spectroscopy (EDS) of the pristine and 1<sup>st</sup> cycle charged and discharged electrodes containing KMO-36h were collected with a high-resolution SEM (JEOL 7600 F) instrument at 20 kV. Prior to measurement, the cycled electrodes were collected, rinsed with solvent, and dried in a glovebox.

**Electrochemical characterization.** A mixture of K<sub>0.9</sub>Mn<sub>8</sub>O<sub>16</sub>, carbon black, and polyvinylidene fluoride (PVDF) cast on aluminum foil was used as the cathode. 1 M LiPF<sub>6</sub> in ethylene carbonate (EC)/dimethyl carbonate (DMC) at a volume ratio of 3:7 was used as the electrolyte. Coin type cells were assembled using the cathode, Li foil, polypropylene separators and electrolyte in an

argon filled glovebox. Cyclic voltammetry (CV) tests were conducted at scan rates of 0.1, 0.2, 0.5, 1, 2 mV/s. For the galvanostatic intermittent titration technique (GITT) tests, a current density of 40 mA/g was applied to a cell for 90 s followed by a 3 hour relaxation time. Rate capability tests were performed at 10 (0.1 C), 20, 50, and 100 mA/g for 10 cycles with a voltage window of 4.0 – 1.5 V. For *ex-situ* XAS measurement samples, galvanostatic cycling tests were controlled to 2 (72 mAh/g) and 4 (144 mAh/g) electron equivalents of discharge at a current density of 50 mA/g. The discharge voltage was limited to 0.5 V, and the charge voltage was limited to 4.0 V. Electrochemical impedance spectra (EIS) were obtained over a frequency range of 1 MHz to 10 mHz, with an AC amplitude of 10 mV using a Bio-Logic potentiostat.

In situ TEM lithiation was performed using a transmission electron microscope (JEM-2100F, JEOL) at an acceleration voltage of 200 kV and a Nanofactory STM-TEM holder. The nano battery was constructed in the TEM. The KMO-36h nanorod cathodes were attached to a half copper grid with conductive epoxy. A lithium metal counter electrode was formed on a sharp tungsten tip via scratching a lithium foil inside a glovebox. The lithium was exposed to air for a few seconds to produce thin Li<sub>2</sub>O coating on the Li tip as a solid electrolyte. After the Li<sub>2</sub>O/Li electrode contacted the nanorods, electrochemical lithiation was initiated by applying a constant potential of -1.0V to the nanorods with respect to the Li counter electrode.

*Ex-situ* XAS. Mn K-edge X-ray absorption spectroscopies (XAS) were collected at 12-BM-B beamline at Argonne National Laboratory. All the samples were sealed between polyimide tapes for measurement. The XAS data analyses were performed using the Athena software packages,  $^{36,37}$  and  $E_0$  value (6.539 keV) from a Mn foil reference was used for all the samples. Edge energy was defined as the maximum of the first derivative of  $\chi\mu(E)$ . Extended X-ray absorption fine structure (EXAFS) of Mn edge was analyzed using the Artemis software packages, and the k range was selected from 2 to 14 Å<sup>-1</sup> with Hanning window type. k,  $k^2$  and  $k^3$  k-weightings were used simultaneously for all fits. K<sub>1.33</sub>Mn<sub>8</sub>O<sub>16</sub> was used as the structure model, <sup>38</sup> and the Mn-O, Mn-Mn<sub>edge</sub> and Mn-Mn<sub>corner</sub> shells were fitted over the R range of 1 to 3.3 Å. The  $k^2$ -weighted EXAFS spectra were displayed in the paper.

#### **Results**

#### Nanotube material characterization

K<sup>+</sup> containing α-MnO<sub>2</sub> (K<sub>x</sub>Mn<sub>8</sub>O<sub>16</sub>) was synthesized using a hydrothermal reaction of KMnO<sub>4</sub> and HCl), where three K<sub>x</sub>Mn<sub>8</sub>O<sub>16</sub> unique sample types were prepared using different reaction times (3h, 12h, and 36h). For simplicity, the three samples are denoted as KMO-3h, KMO-12h, and KMO-36h, respectively. A previous theoretical study on α-MnO<sub>2</sub> indicated that the surface energy of (001) plane is 1.76 J/m<sup>2</sup>, which is 2-3 times higher than that of (100) and (110) plane.<sup>39</sup> When the width of K<sub>0.9</sub>Mn<sub>8</sub>O<sub>16</sub> nanorod is large, Cl-containing species in the solution may corrode the (001) surface of K<sub>0.9</sub>Mn<sub>8</sub>O<sub>16</sub> nanorod to reduce the surface energy, leading to a nanotube morphology. The formation mechanism of the hollow region in K<sub>x</sub>Mn<sub>8</sub>O<sub>16</sub> nanorod was also experimentally investigated, and *ex-situ* SEM images of K<sub>x</sub>Mn<sub>8</sub>O<sub>16</sub> nanorods at different reaction times have shown the hollow region increases with increasing reaction time from 160 min to 180 min.<sup>33</sup> Thus, nanotube K<sub>0.9</sub>Mn<sub>8</sub>O<sub>16</sub> materials with variation in the hollow region were synthesized in a facile manner by increasing the reaction time in HCl solution.

The three samples have similar XRD patterns which are indexed to tetragonal (PDF # 01-077-1796). There are only minor changes in peak positions and peak intensities, implying similar crystal structure and crystallinity (**Fig. 1a-c**). Rietveld refinement was performed to obtain specific structural information, and the refined results for KMO-3h, KMO-12h, and KMO-36h show similar lattice parameter a of 9.8121, 9.8131 and 9.8133 Å, respectively. The similar lattice parameters and unit cell volumes (**Fig. 1a-c**) indicate that the reaction time has minor impact on the parent unit cell structure. The central K<sup>+</sup> content was determined using inductively coupled plasma optical emission spectroscopy (ICP-OES), and all three samples have the same K/8Mn ratio of 0.9. The thermal stability and water content were determined by TGA (**Fig. S1**). Weight losses of ~1.5% are observed for the three samples at temperatures below 350 °C, which are assigned to physisorbed and chemisorbed water. Based on the TGA results, the samples contain ~0.7H<sub>2</sub>O per K<sub>0.9</sub>Mn<sub>8</sub>O<sub>16</sub> formula unit. The weight losses starting at ~450 °C, correspond to the decomposition of the materials to Mn<sub>2</sub>O<sub>3</sub> and Mn<sub>3</sub>O<sub>4</sub>.

Mn K-edge X-ray absorption near edge structure (XANES) and extended X-ray absorption fine structure (EXAFS) were utilized to analyze average Mn oxidation state and local coordination environment for the three sample types (**Fig.1d** and **1e**). KMO-3h, KMO-12h, and KMO-36h show similar Mn edge energies at ~6557.2 eV, indicating similar Mn oxidation states in the bulk samples. The Fourier transformed EXAFS results show three intense peaks, corresponding to Mn-O, edge-sharing Mn-Mn, and corner-sharing Mn-Mn scattering. The fitted results indicate that the three samples have similar atomic distances of ~1.91 Å (Mn-O), ~2.86/2.90 Å (Mn-Mn\_edge\_c/ Mn-Mn\_edge\_ab), and ~3.42 Å (Mn-Mn\_corner), **Table S2**. Thus, longer reaction time shows little impact on the parent structures of K<sub>0.9</sub>Mn<sub>8</sub>O<sub>16</sub> samples, consistent with the XRD results.

Material microstructures were investigated using STEM imaging, Fig. 2 and Fig. S2. The morphological feature of a selected nanotube along [100] direction for the KMO-3h sample is shown in Fig. 2a. The dark contrast in the interior corresponds to the hollowed regions within the nanotube since the contrast of HAADF imaging is very sensitive the atomic number and thickness. The width of the hollowed region is around 10 nm. In order to reveal the variation of valence state of Mn across the nanotube, we performed the spectrum imaging analyses along the indicated arrowed line. As shown in **Fig. 2b**, the energy positions of the Mn- $L_2$  edge, Mn- $L_3$ edge, L<sub>3</sub>/L<sub>2</sub> ratio and associated thickness were extracted. It is seen that there is no obvious energy shift of Mn- $L_{2,3}$  positions from surface to interior and the white line ratio of  $L_3/L_2$  also does not have obvious changes. Therefore, there are no obvious oxygen vacancies along the surfaces as oxygen vacancies are closely related to the shift of Mn-L<sub>2,3</sub> positions and the variation of white line ratio. 42-44 For the nanotube in KMO-12h sample, as shown in **Fig. 2c**, the width of the hollowed region is around 30 nm, which is larger than that of the nanotube in the KMO-3h sample. Detailed EELS analyses shown in Fig. 2d reveals that the surface phenomenon become obvious as we can see the energy shift of Mn-L<sub>2,3</sub> positions and variation of white line ratio. The total width of the surface region is around 5 nm. Fig. 2e HAADF image shows the microstructural feature of the nanotube in KMO-36h sample. The width of the hollowed region is around 30 nm. Based on Fig. 2f EELS analyses, it is found that the oxygen vacancy is more apparent on the outer surfaces as there is obvious energy shift of Mn-L<sub>2,3</sub> positions and variation of white line ratio. The total width of the surface region is around 10 nm, about 2 times of that of the KMO-12h sample although the width of the nanotube shown in Fig. 2c and Fig. 2c are similar. Additionally, we can see clear energy shift of Mn- $L_{2,3}$  positions around the inner surface

in the KMO-36h sample as indicated by the circles. Thus, oxygen vacancies occur not only around the outmost surfaces but also the inter surface inside the nanotube. Comparisons of the microstructural and chemical features shown in **Fig. 2**, reveal that the longer reaction time results in larger hollowed regions and enlarges the surface regions that are decorated by oxygen vacancies.

Surface elemental compositions and Mn oxidation states were analyzed using XPS, Fig. 3, Fig. S3 and Table S3. Survey spectra of KMO samples synthesized under different reaction times show characteristic peaks of Mn 2p, O 1s, K 2p, and Mn 3s. O 1s spectra were used to probe the surface oxygen composition, Fig. 3a. A prior report on electron escape length in XPS indicated the sampling depth is <6 nm for most elements at 500 eV electron energy<sup>45</sup>, so the O 1s spectra represent the outer surface information for the KMO nanotubes. The peak in the O 1s spectral region was fitted using three components, corresponding to Mn-O-Mn (~530 eV), Mn-O-H (~531 eV), and H-O-H (~533 eV). The peak positions are in agreement with reported values for potassium containing  $\alpha$ -MnO<sub>2</sub>. <sup>30,46,47</sup> The fitted results indicate the content of lattice oxygen (Mn-O-Mn) decreases from 70% to 65% while the content of hydroxy oxygen (Mn-O-H) slightly increases from 21% to 22% from KMO-3h to KMO-36h. Therefore, the ratio of Mn-O-H species to Mn-O-Mn in KMO-36h (0.34) is higher than that in KMO-3h (0.30), indicative of a higher level of surface defects. The spectral splitting ( $\Delta E_{Mn3s}$ ) in the Mn 3s spectra (**Fig. 3b**) can be used to estimate surface Mn oxidation state according to a linear correlation (Mn valence = 8.956 –  $1.126 \times \Delta E_{Mn3s}$ ).  $^{30,46,47}$  The estimated Mn oxidation states are 3.78, 3.79, and 3.75 for KMO-3h, KMO-12h, and KMO-36h, respectively. The lower Mn oxidation states compared to the nominal Mn oxidation state for stoichiometric K<sub>0.9</sub>Mn<sub>8</sub>O<sub>16</sub> (3.89) can be attributed to surface defects, also consistent with the surface defects results determined by the EELS characterization.

#### **Electrochemistry**

Material redox properties and lithiation/de-lithiation kinetics of Li/  $K_{0.9}Mn_8O_{16}$  cells were investigated using cyclic voltammetry measurements at scan rates of 0.1, 0.2, 0.5, 1.0, and 2.0 mV/s, **Fig. 4a-c**. The three KMO electrodes all show one major redox couple in the voltage range of 4.0 - 2.2 V. The ΔEpeak values at all scan rates show a trend with KMO-3h > KMO-12h > KMO-36h (**Table S4**). At 0.1 mV/s, ΔE values of KMO-3h, KMO-12h, and KMO-36h are 0.47, 0.44, 0.38 V, respectively. When the scan rate increases to 2 mV/s, the value of ΔE for KMO-3h and KMO-12H is 1.89 and 1.64 V, respectively, while that for KMO-36h is 1.22 V. The larger ΔE value at the high scan rate for KMO-3h and KMO-12h indicates overall slower Li<sup>+</sup> transport compared to the KMO-36h sample. The average effective Li<sup>+</sup> ion diffusion coefficients (D<sub>Li+</sub>) were estimated based on the CV results (**Supplementary Note 1** and **Fig. S4**) as  $7.8 \times 10^{-13}$ ,  $1.4 \times 10^{-12}$ , and  $2.0 \times 10^{-12}$  cm<sup>2</sup>/s, for KMO-3h, KMO-12h, and KMO-36h, respectively.

The change in effective  $D_{Li^+}$  upon lithiation was probed using Galvanostatic intermittent titration technique (GITT) type measurements. The three samples display similar quasi-equilibrium opencircuit voltages throughout the lithiation process (0 – 3 electron equivalents per  $K_{0.9}Mn_8O_{16}$ ), indicative of the same thermodynamic potential in the samples. However, the loaded voltage of KMO-36h is higher than that of KMO-3h and KMO-12h in the initial lithiation process (0 – 1 electron equivalent), **Fig. 4d**. The effective  $D_{Li^+}$  values were estimated at different lithiation levels based on the GITT results (**Fig. 4e** and **Supplementary Note 2**). From 0 – 0.3 electron equivalents, the effective  $D_{Li^+}$  value decreases from ~1×10<sup>-9</sup> to ~1×10<sup>-11</sup> cm<sup>2</sup>/s, and the second

decrease ( $\sim 1 \times 10^{-11}$  to  $\sim 1 \times 10^{-13}$  cm<sup>2</sup>/s) occurs from 1.5 – 2.5 electron equivalents. The decreasing trend of effective  $D_{Li+}$  has also been observed in other reports on  $K_xMn_8O_{16}$  type materials. Notably, at low levels of lithiation, < 0.2 Li<sup>+</sup> ion equivalents, the effective  $D_{Li+}$  value of KMO-36h is  $\sim 1$  order of magnitude higher than that of KMO-3h, **inset Fig. 4e**. The  $D_{Li+}$  values of the three samples are more similar after  $\sim 1$  electron equivalent, in agreement with their similar load voltages after 1 molar equivalent of lithiation.

The cells containing the KMO samples were tested at different current levels to investigate the impact on the delivered capacity (**Fig. 4f**). At 0.1 C, the capacities of KMO-3h, KMO-12h, and KMO-36h are 130, 140, and 150 mAh/g, respectively. When the cycling rate increases to 0.5 C, the capacity of KMO-3h is 48 mAh/g, while KMO-36h delivers a capacity of 89 mAh/g. The larger capacities in KMO-36h relative to KMO-3h are attributed to the improved effective Li<sup>+</sup> ion diffusion. The discharge/charge curves and dQ/dV plots show that the three samples have similar voltage profiles at 0.1 C rate and increased polarization at 0.5 C rate (**Fig. S5**). The KMO-3h sample displays the largest polarization and the most significant capacity decrease at high rate. Capacity retention under the different rates is compared in the **inset in Fig. 4f**. At 0.2 C, 0.5 C and 1 C, KMO-36h maintains 85%, 60%, and 34% of the capacity delivered at 0.1 C, respectively. In contrast, the capacity retention of KMO-3h is only 72%, 37%, and 17% from 0.2 C to 1 C with the rate capability of KMO-12h between the other two samples.

#### In situ visualization of lithium-ion transport

The lithium transport in a hollow KMO-36h nanorod was investigated and visualized via in situ TEM. The lithium ion mobility and associated nanorod expansion propagated along the longitudinal direction starting from the point of contact with the lithium tip (**Fig. 5a**). Upon applying a bias potential of -1 V to the nanorod, we observed changes in the interior contrast of the nanorod where many needle-like regions became visible, **Fig. 5b–d**. The lithium-ion transport observed was a fast process with a small net volume change of the nanorod also observed. After 3 s, a distinct lithiation reaction front (RF) appeared, characterized by substantial cross-sectional expansion, and ~31% volume expansion from 134 nm to 175 nm (**Fig. 5a-f and supplementary movie S1**). The RF propagated ~521nm within 180 s, corresponding to ~2.9 nm s<sup>-1</sup>. The fast process and lithiation RF is consistent with the previous observation of in situ lithiation of Ag<sub>1.6</sub>Mn<sub>8</sub>O<sub>16</sub> nanorods.<sup>29</sup> Interestingly, the dimension (~28 nm) of the hollow section near the center of the nanorod of the KMO-36h nanorod material did not change during the in situ lithiation process.

#### **Analysis of cycled materials**

Cells containing the KMO samples were cycled under controlled reduction of 2 and 4 molar electron equivalents (2e and 4e). The terminal discharge voltages are utilized to analyze the reversibility under the two reduction conditions (**Fig. 6a**). Under the 2e reduction condition, the terminal voltages decrease from ~2.1 V to ~1.5 V in the initial 3 cycles with low Coulombic efficiencies (~60% in the first cycle, **Fig. S6a**). The Coulombic efficiencies of the three samples all remained near 100% after cycle 3, and the terminal voltages stabilized at ~1.5 V. Under the 4 electron equivalent reduction condition, the three samples also show terminal voltage decrease and low Coulombic efficiencies in the initial cycles (**Fig. S6b**). Due to lower Li<sup>+</sup> ion diffusion in KMO-3h, the terminal voltage of this sample is 0.78 V at cycle 1, significantly lower than ~1.3 V for KMO-12h and KMO-36h. The KMO-3h cell reaches the discharge limit (0.5 V) at cycle 2, and fails to achieve 4e reduction (1.2e – 3.3e) in the following cycles. In contrast, both KMO-

12h and KMO-36h show only minor terminal voltage decrease (1.3 to 1.1 V) in the initial 10 cycles. It is notable that a significant voltage decrease occurs at cycle 15 for the KMO-12h cell. The terminal voltage of KMO-12h fades to 0.5 V at cycle 20 while that of KMO-36h is maintained at 1.0 V. Discharge-charge profiles at cycle 2 and cycle 20 are compared to show the change in polarization after cycling (**Fig. 6b**). KMO-12h and KMO-36h have almost identical voltage profiles at cycle 2, while KMO-3h shows a lower discharge voltage and higher charge voltage. After 20 cycles, the KMO-36h cell maintains a similar voltage profile, however, the KMO-12h cell shows increased polarization. CV, GITT, and rate capability tests show the KMO sample with the larger and defective hollow region has improved lithiation kinetics.

The AC impedance of KMO samples before (solid line) and after (dashed line) 20 cycles under 4 e and 2 e reduction were collected, as shown in **Fig. 6c and Fig. S7** respectively. AC Impedance results indicate that KMO-12h and KMO-36h have similar Nyquist plots before cycling under 4 e reduction while KMO-3h shows a larger semicircle in the Nyquist plot (**Fig. 6c**). The impedance data were fitted using a Randles circuit (**Fig. S7a**). Before cycling, KMO-3h shows a large charge transfer resistance (Rct) of 490 ohm, which is >3 times higher than that of KMO-12h (150 ohm) and KMO-36h (148 ohm), **Table S5**. After 20 cycles under 2e reduction (**Fig. S7b**), the three KMO samples all show increased Rct values. KMO-12h and KMO-36h have similar Rct values (~400 ohm), and the Rct value of KMO-3h increases to 1047 ohm. After 20 cycles under 4e reduction, the Rct values increase to 9202, 4467, and 928 ohms in KMO-3h, KMO-12h, and KMO-36h, respectively. The large impedance values of KMO-3h and KMO-12h after 20 cycles are consistent with the increased polarization observed in Coulombically-controlled galvanostatic cycling.

X-ray absorption spectroscopy was used to gain further insight into the oxidation state and structure of the materials after cycling. Mn K-edge x-ray absorption near edge spectra (XANES) of the charged KMO electrodes were investigated. After 20 cycles under 2e reduction, the three samples have similar Mn edge energies, which are slightly smaller (0.4 eV) than 6557.2 eV that was observed for the as prepared material (Fig. S8). However, there are notable edge energy shifts after 20 cycles under 4e reduction (**Fig. 6d**). The edge energies of the charged KMO-3h and KMO-12h electrodes shift to 6555.8 eV, indicating reduced Mn oxidation states in the two samples even after charge. The edge energy of the charged KMO-36h electrode is 6556.3 eV. Thus, the KMO-36h sample displays a higher Mn oxidation state than the other two samples after cycling, consistent with the higher Coulombic efficiency of KMO-36h under cycling. The EXAFS region was used to analyze the local structure change after cycling (Fig. 6e and Fig. S8). After 20 cycles under 2e reduction, the extended x-ray absorption fine structure (EXAFS) spectra of the three charged electrodes show similar peak positions and intensities to the spectra of undischarged electrodes. However, at the 4e molar electron equivalent cycling after 20 cycles, new peaks occur at ~2.7 Å in the charged KMO spectra, showing Mn-Mn distortion. Moreover, the peak amplitudes at ~3.0 Å (Mn-Mn<sub>corner</sub>) show apparent decreases in the spectra of the three charged KMO electrodes.

The spectra were fitted using the Mn-O, Mn-Mn<sub>edge</sub>, and Mn-Mn<sub>corner</sub> shells. In the  $K_{1.33}Mn_8O_{16}$  structure, the Mn-Mn<sub>edge</sub> shell consists of two types of Mn-Mn paths with one in lattice in the c direction (Mn-Mn<sub>edge\_c</sub>) and the other one in the ab plane (Mn-Mn<sub>edge\_ab</sub>). A prior study on a silver ion containing  $\alpha$ -MnO<sub>2</sub> (Ag<sub>1.2</sub>Mn<sub>8</sub>O<sub>16</sub>) indicated that Mn-Mn<sub>edge\_c</sub> distance shows minor change while Mn-Mn<sub>edge\_ab</sub> distance shows a ~0.14 Å increase when Ag<sub>1.2</sub>Mn<sub>8</sub>O<sub>16</sub> is lithiated to Li<sub>4</sub>Ag<sub>1.2</sub>Mn<sub>8</sub>O<sub>16</sub>. Thus, the new peak (~2.7 Å) can be attributed to the elongated Mn-Mn<sub>edge</sub> ab

distance. The EXAFS data simulations show reasonable fits with R factors < 0.018. After 20 cycles under 2e reduction, there are no apparent increases in atomic distances. The Mn-O distances are  $1.91 \pm 0.01$  Å and the Mn-Mn<sub>edge</sub> ab distances are  $2.91 \pm 0.01$  Å in the charged KMO-3h, KMO-12h, and KMO-36h electrodes. After 20 cycles under 4e reduction, the Mn-O distances (1.91 – 1.92 Å) are similar in the charged electrodes. The Mn-Mn<sub>edge</sub> ab distances are  $2.92 \pm 0.02$  Å,  $2.93 \pm 0.01$  Å, and  $2.91 \pm 0.02$  Å in KMO-3h, KMO-12h, and KMO-36h, respectively. In comparison to the Mn-Mn<sub>edge\_</sub>ab distances  $(2.90 \pm 0.01 \text{ Å})$  in the undischarged KMO electrodes, the increases in the atomic distances after cycling are not significant. However, large decreases in Mn-O near neighbors after cycling under 4e reduction are observed. The near neighbors of Mn-O decreases from  $5.9 \pm 0.5$  to  $4.4 \pm 0.2$ ,  $6.0 \pm 0.5$  to  $4.0 \pm 0.3$ , and  $5.9 \pm 0.5$  to  $3.9 \pm 0.4$  for KMO-3h, KMO-12h, and KMO-36h, respectively. The fitted Debye-Waller factors (Mn-O path) for all the spectra are ~0.004, indicating the decreased peak amplitudes in the EXAFS spectra are due to the decreased near neighbors. The Mn-O near neighbors in the charged KMO electrodes are not recovered to ~6, suggesting irreversible structural change under 4e reduction. The XRD patterns indicate that the materials become largely amorphous after 20 cycles under 4e reduction (Fig. S9), consistent with the XAS results.

Under repetitive 4e reduction, the three KMO electrodes all show decreases in terminal discharge voltages. The decreased terminal voltage is correlated with the structural change under lithiation/de-lithiation (4e). XAS and XRD of the charged KMO electrodes indicate the materials become amorphous after cycling, and the amorphization may be due to large unit cell expansion at high lithiation level (K<sup>+</sup>-Li<sub>4</sub>Mn<sub>8</sub>O<sub>16</sub>). Previous theoretical and experimental studies on  $\alpha$ -MnO<sub>2</sub> type materials indicate there is a large unit cell volume (atomic distance) expansion (7%-15%) at Li<sub>0.5</sub>MnO<sub>2</sub> or Li<sub>4</sub>Mn<sub>8</sub>O<sub>16</sub> due to the Jahn-Teller distortion. <sup>43,50-52</sup> It is notable that the terminal voltage of KMO-3h reaches the 0.5 V discharge voltage limit after only 2 cycles. KMO-12h shows a 0.8 V decrease in terminal discharge voltage after 20 cycles while KMO-36h shows a 0.3 V decrease. The hollow regions in the particles proved to be conducive to material structural and electrochemical stability. Further, the increased size of the hollow regions and the oxygen vacancies in the KMO-36h sample facilitate the ionic transport as previously observed in  $\alpha$ -MnO<sub>2</sub> type materials. <sup>27,43</sup>

The morphology and elemental analysis of a pristine electrode and electrodes after discharge and charge at 0.1C and 0.5C under 4 molar electron equivalents were characterized by SEM/EDS (Figure S10). The hollow nanotube morphology is maintained after the first discharge and charge at 0.1C and 0.5C based on the SEM images. The Mn/K atomic ratios were calculated from the EDS spectra. The Mn/K atomic ratio of cycled electrode remained at 8.7: 1 and did not significantly change compared to the pristine electrode and the original  $K_{0.9}Mn_8O_{16}$  material with an Mn/K atomic ration of 8.8:1. Collectively, the morphology and elemental composition of KMO materials are stable after the first discharge and charge at two different current rates.

#### **Conclusion**

A facile hydrothermal method to prepare  $K_{0.9}Mn_8O_{16}$  nanotubes was demonstrated where the reaction time can be used to increase the hollow region size and the level of surface defect region in the nanotubes. The  $K_{0.9}Mn_8O_{16}$  sample with the longer reaction time (KMO-36h) showed a larger hollow region compared to KMO-3h and a higher level of surface defects compared to

KMO-12h. The total width of the surface defect region was observed to be 5 nm and 10 nm for KMO-12h and KMO-3h, respectively, as verified by EELS. KMO-36h showed a 0.7 V lower ΔE peak value at 2 mV/s than KMO-3h by CV, and ~1 order of magnitude higher effective lithium ion diffusion coefficients in the initial lithiation process by GITT. The higher lithiation kinetics in KMO-36h in relative to KMO-3h can be associated with the larger hollow region size and the higher level of surface defects. In situ lithiation was conducted to enable visualization of the lithiation process. With lithiation, the nanorod expansion propagated in the longitudinal direction, however, the dimension (~28 nm) of the hollow section near the center of the nanorod material did not change during the in situ lithiation process. This study illustrates the opportunity for tuning material morphology to facilitate lithium ion diffusion. In this case, controlled synthesis enabled the deliberate creation of materials with larger hollow dimensions and greater defects in the particle hollow regions yielding enhanced electrochemistry, particularly at high rate.

#### Acknowledgement

This work was supported as part of the Center for Mesoscale Transport Properties, an Energy Frontier Research Center supported by the U.S. Department of Energy, Office of Science, Basic Energy Sciences, under award #DE-SC0012673. The synchrotron-based XRD data were collected at the National Synchrotron Light Source II, Brookhaven National Laboratory supported by the Department of Energy, under Contract No. DE-SC0012704. The X-ray absorption spectroscopy measurements were conducted at Beamline 12-BM-B of the Advanced Photon Source at Argonne National Laboratory supported by the Department of Energy, under Contract No. DE-AC02-06CH11357. The XPS, in situ TEM and SEM experiments were carried out at the Center for Functional Nanomaterials at Brookhaven National Laboratory supported by the Department of Energy, Office of Basic Energy Sciences, under Contract No. DE-AC02-98CH10886. EST acknowledges the support of the William and Jane Knapp Chair of Energy and the Environment.

#### References

- (1) Thackeray, M. M. Manganese oxides for lithium batteries. *Progress in Solid State Chemistry* **1997**, 25, 1-71.
- (2) Housel, L. M.; Wang, L.; Abraham, A.; Huang, J.; Renderos, G. D.; Quilty, C. D.; Brady, A. B.; Marschilok, A. C.; Takeuchi, K. J.; Takeuchi, E. S. Investigation of α-MnO2 Tunneled Structures as Model Cation Hosts for Energy Storage. *Accounts of Chemical Research* **2018**.
- (3) Wu, D.; Housel, L. M.; Kim, S. J.; Sadique, N.; Quilty, C. D.; Wu, L.; Tappero, R.; Nicholas, S. L.; Ehrlich, S.; Zhu, Y. Quantitative temporally and spatially resolved X-ray fluorescence microprobe characterization of the manganese dissolution-deposition mechanism in aqueous  $Zn/\alpha$ -MnO 2 batteries. *Energy & Environmental Science* **2020**, *13*, 4322-4333.
- (4) Tsai, Y.-C.; Kuo, C.-T.; Liu, S.-F.; Lee, Y.-T.; Yew, T.-R. Effect of Different Electrolytes on MnO2 Anodes in Lithium-Ion Batteries. *The Journal of Physical Chemistry C* **2021**, *125*, 1221-1233.

- (5) Yang, R.; Fan, Y.; Ye, R.; Tang, Y.; Cao, X.; Yin, Z.; Zeng, Z. MnO2 Based Materials for Environmental Applications. *Advanced Materials* **2021**, *33*, 2004862.
- (6) Suib, S. L. Porous Manganese Oxide Octahedral Molecular Sieves and Octahedral Layered Materials. *Accounts of Chemical Research* **2008**, *41*, 479-487.
- (7) Su, D.; Ahn, H.-J.; Wang, G. Hydrothermal synthesis of [small alpha]-MnO2 and [small beta]-MnO2 nanorods as high capacity cathode materials for sodium ion batteries. *Journal of Materials Chemistry A* **2013**, *1*, 4845-4850.
- (8) Poyraz, A. S.; Huang, J.; Cheng, S.; Wu, L.; Tong, X.; Zhu, Y.; Marschilok, A. C.; Takeuchi, K. J.; Takeuchi, E. S. Tunnel Structured α-MnO2 with Different Tunnel Cations (H+, K+, Ag+) as Cathode Materials in Rechargeable Lithium Batteries: The Role of Tunnel Cation on Electrochemistry. *Journal of The Electrochemical Society* **2017**, *164*, A1983-A1990.
- (9) Zhang, R.; Yu, X.; Nam, K.-W.; Ling, C.; Arthur, T. S.; Song, W.; Knapp, A. M.; Ehrlich, S. N.; Yang, X.-Q.; Matsui, M. α-MnO2 as a cathode material for rechargeable Mg batteries. *Electrochemistry Communications* **2012**, *23*, 110-113.
- (10) Zhang, R.; Arthur, T. S.; Ling, C.; Mizuno, F. Manganese dioxides as rechargeable magnesium battery cathode; synthetic approach to understand magnesiation process. *Journal of Power Sources* **2015**, 282, 630-638.
- (11) Huang, J.; Poyraz, A. S.; Lee, S.-Y.; Wu, L.; Zhu, Y.; Marschilok, A. C.; Takeuchi, K. J.; Takeuchi, E. S. Silver-Containing α-MnO2 Nanorods: Electrochemistry in Na-Based Battery Systems. *ACS Applied Materials & Interfaces* **2017**, *9*, 4333-4342.
- (12) Huang, J.; Poyraz, A. S.; Takeuchi, K. J.; Takeuchi, E. S.; Marschilok, A. C. MxMn8O16 (M = Ag or K) as promising cathode materials for secondary Mg based batteries: the role of the cation M. *Chemical Communications* **2016**, *52*, 4088-4091.
- (13) Pan, H.; Shao, Y.; Yan, P.; Cheng, Y.; Han, K. S.; Nie, Z.; Wang, C.; Yang, J.; Li, X.; Bhattacharya, P.; Mueller, K. T.; Liu, J. Reversible aqueous zinc/manganese oxide energy storage from conversion reactions. *Nature Energy* **2016**, *1*, 16039.
- (14) Xu, C.; Li, B.; Du, H.; Kang, F. Energetic zinc ion chemistry: the rechargeable zinc ion battery. *Angewandte Chemie International Edition* **2012**, *51*, 933-935.
- (15) Ismail, A.; Prabowo, H. A.; Alfaruqi, M. H. Potassium-Intercalated Manganese Dioxide as Lithium-ion Battery Cathodes: A Density Functional Theory Study. *Sinergi* **2019**, *23*, 55-60.
- (16) Kim, S. J.; Wu, D.; Sadique, N.; Quilty, C. D.; Wu, L.; Marschilok, A. C.; Takeuchi, K. J.; Takeuchi, E. S.; Zhu, Y. Unraveling the Dissolution Mediated Reaction Mechanism of α MnO2 Cathodes for Aqueous Zn Ion Batteries. *Small* **2020**, *16*, 2005406.
- (17) Cao, Z.; Yang, Y.; Qin, J.; He, J.; Su, Z. Co3O4 Polyhedron@ MnO2 Nanotube Composite as Anode for High Performance Lithium Ion Batteries. *Small* **2021**, *17*, 2008165.
- (18) Wang, Z.; Yan, X.; Wang, F.; Xiong, T.; Balogun, M.-S.; Zhou, H.; Deng, J. Reduced graphene oxide thin layer induced lattice distortion in high crystalline MnO2 nanowires for high-performance sodium-and potassium-ion batteries and capacitors. *Carbon* **2021**, *174*, 556-566.
- (19) Zhu, X.; Cao, Z.; Wang, W.; Li, H.; Dong, J.; Gao, S.; Xu, D.; Li, L.; Shen, J.; Ye, M. Superior-Performance Aqueous Zinc-Ion Batteries Based on the In Situ Growth of MnO2 Nanosheets on V2CTX MXene. *ACS nano* **2021**, *15*, 2971-2983.
- (20) Cao, Z.; Yang, Y.; Qin, J.; Su, Z. A core-shell porous MnO2/Carbon nanosphere composite as the anode of lithium-ion batteries. *Journal of Power Sources* **2021**, *491*, 229577.

- (21) Zhang, D.; Li, Z.; Li, Y.; Zeng, P.; Shu, H.; Chen, M.; Wang, X. Hollow urchin-like Al-doped α-MnO2– x as advanced sulfur host for high-performance lithium-sulfur batteries. *Materials Letters* **2021**, 285, 129135.
- (22) Li, B.; Rong, G.; Xie, Y.; Huang, L.; Feng, C. Low-temperature synthesis of α-MnO2 hollow urchins and their application in rechargeable Li+ batteries. *Inorganic chemistry* **2006**, *45*, 6404-6410.
- (23) Guo, X.; Li, J.; Jin, X.; Han, Y.; Lin, Y.; Lei, Z.; Wang, S.; Qin, L.; Jiao, S.; Cao, R. A hollow-structured manganese oxide cathode for stable Zn-MnO2 batteries. *Nanomaterials* **2018**, *8*, 301.
- (24) Chen, H.; Dong, W.-D.; Xia, F.-J.; Zhang, Y.-J.; Yan, M.; Song, J.-P.; Zou, W.; Liu, Y.; Hu, Z.-Y.; Liu, J. Hollow nitrogen-doped carbon/sulfur@ MnO2 nanocomposite with structural and chemical dual-encapsulation for lithium-sulfur battery. *Chemical Engineering Journal* **2020**, *381*, 122746.
- (25) Yang, Y.; Ma, G.; Huang, J.; Nan, J.; Zhen, S.; Wang, Y.; Li, A. Hollow MnO2 spheres/porous reduced graphene oxide as a cathode host for high-performance lithium-sulfur batteries. *Journal of Solid State Chemistry* **2020**, 286, 121297.
- (26) Bi, R.; Liu, G.; Zeng, C.; Wang, X.; Zhang, L.; Qiao, S. Z. 3D Hollow a MnO2 Framework as an Efficient Electrocatalyst for Lithium Oxygen Batteries. *Small* **2019**, *15*, 1804958.
- (27) Wu, L.; Xu, F.; Zhu, Y.; Brady, A. B.; Huang, J.; Durham, J. L.; Dooryhee, E.; Marschilok, A. C.; Takeuchi, E. S.; Takeuchi, K. J. Structural Defects of Silver Hollandite, AgxMn8Oy, Nanorods: Dramatic Impact on Electrochemistry. *ACS Nano* **2015**, *9*, 8430-8439.
- (28) Hu, X.; Huang, J.; Wu, L.; Kaltak, M.; Fernandez-Serra, M. V.; Meng, Q.; Wang, L.; Marschilok, A. C.; Takeuchi, E. S.; Takeuchi, K. J. Atomic scale account of the surface effect on ionic transport in silver hollandite. *Chemistry of Materials* **2018**, *30*, 6124-6133.
- (29) Xu, F.; Wu, L.; Meng, Q.; Kaltak, M.; Huang, J.; Durham, J. L.; Fernandez-Serra, M.; Sun, L.; Marschilok, A. C.; Takeuchi, E. S.; Takeuchi, K. J.; Hybertsen, M. S.; Zhu, Y. Visualization of lithium-ion transport and phase evolution within and between manganese oxide nanorods. *Nature Communications* **2017**, *8*, 15400.
- (30) Lee, S.-Y.; Wu, L.; Poyraz, A. S.; Huang, J.; Marschilok, A. C.; Takeuchi, K. J.; Takeuchi, E. S.; Kim, M.; Zhu, Y. Lithiation Mechanism of Tunnel-Structured MnO2 Electrode Investigated by In Situ Transmission Electron Microscopy. *Advanced Materials* **2017**, 29, 1703186-n/a.
- (31) Cai, R.; Guo, S.; Meng, Q.; Yang, S.; Xin, H. L.; Hu, X.; Li, M.; Sun, Y.; Gao, P.; Zhang, S. Atomic-level tunnel engineering of todorokite MnO2 for precise evaluation of lithium storage mechanisms by in situ transmission electron microscopy. *Nano Energy* **2019**, *63*, 103840.
- (32) Lee, S.-Y.; Housel, L. M.; Huang, J.; Wu, L.; Takeuchi, E. S.; Marschilok, A. C.; Takeuchi, K. J.; Kim, M.; Zhu, Y. Inhomogeneous structural evolution of silver-containing Alpha-MnO2 nanorods in sodium-ion batteries investigated by comparative transmission electron microscopy approach. *Journal of Power Sources* **2019**, *435*, 226779.
- (33) Luo, J.; Zhu, H. T.; Fan, H. M.; Liang, J. K.; Shi, H. L.; Rao, G. H.; Li, J. B.; Du, Z. M.; Shen, Z. X. Synthesis of Single-Crystal Tetragonal α-MnO2 Nanotubes. *The Journal of Physical Chemistry C* **2008**, *112*, 12594-12598.

- (34) Toby, B. H.; Von Dreele, R. B. GSAS-II: the genesis of a modern open-source all purpose crystallography software package. *Journal of Applied Crystallography* **2013**, *46*, 544-549.
- (35) Pearson, D. H.; Ahn, C. C.; Fultz, B. White lines and d-electron occupancies for the 3d and 4d transition metals. *Physical Review B* **1993**, *47*, 8471-8478.
- (36) Ravel, B.; Newville, M. ATHENA, ARTEMIS, HEPHAESTUS: data analysis for X-ray absorption spectroscopy using IFEFFIT. *Journal of synchrotron radiation* **2005**, *12*, 537-541.
- (37) Ravel, B.; Newville, M. ATHENA and ARTEMIS: interactive graphical data analysis using IFEFFIT. *Physica Scripta* **2005**, 2005, 1007.
- (38) Vicat, J.; Fanchon, E.; Strobel, P.; Tran Qui, D. The structure of K1. 33Mn8O16 and cation ordering in hollandite-type structures. *Acta Crystallographica Section B: Structural Science* **1986**, *42*, 162-167.
- (39) Tompsett, D. A.; Parker, S. C.; Islam, M. S. Surface properties of  $\alpha$ -MnO 2: relevance to catalytic and supercapacitor behaviour. *Journal of Materials Chemistry A* **2014**, 2, 15509-15518.
- (40) Kijima, N.; Yasuda, H.; Sato, T.; Yoshimura, Y. Preparation and characterization of open tunnel oxide α-MnO2 precipitated by ozone oxidation. *Journal of Solid State Chemistry* **2001**, *159*, 94-102.
- (41) Chen, J.; Tang, X.; Liu, J.; Zhan, E.; Li, J.; Huang, X.; Shen, W. Synthesis and Characterization of Ag– Hollandite Nanofibers and Its Catalytic Application in Ethanol Oxidation. *Chemistry of materials* **2007**, *19*, 4292-4299.
- (42) Wu, L.; Xu, F.; Zhu, Y.; Brady, A. B.; Huang, J.; Durham, J. L.; Dooryhee, E.; Marschilok, A. C.; Takeuchi, E. S.; Takeuchi, K. J. Structural defects of silver hollandite, Ag<sub>x</sub>Mn<sub>8</sub>O<sub>y</sub>, nanorods: dramatic impact on electrochemistry. *ACS Nano* **2015**, *9*, 8430-8439.
- (43) Hu, X.; Huang, J.; Wu, L.; Kaltak, M.; Fernandez-Serra, M. V.; Meng, Q.; Wang, L.; Marschilok, A. C.; Takeuchi, E. S.; Takeuchi, K. J.; Hybertsen, M. S.; Zhu, Y. Atomic Scale Account of the Surface Effect on Ionic Transport in Silver Hollandite. *Chemistry of Materials* **2018**, *30*, 6124-6133.
- (44) Hu, X.; Kitchaev, D. A.; Wu, L.; Zhang, B.; Meng, Q.; Poyraz, A. S.; Marschilok, A. C.; Takeuchi, E. S.; Takeuchi, K. J.; Ceder, G.; Zhu, Y. Revealing and rationalizing the rich polytypism of todorokite MnO<sub>2</sub>. *Journal of the American Chemical Society* **2018**, *140*, 6961-6968.
- (45) Werner, W. Towards a universal curve for electron attenuation: Elastic scattering data for 45 elements. *Surface and interface analysis* **1992**, *18*, 217-228.
- (46) Yan, W.; Ayvazian, T.; Kim, J.; Liu, Y.; Donavan, K. C.; Xing, W.; Yang, Y.; Hemminger, J. C.; Penner, R. M. Mesoporous manganese oxide nanowires for high-capacity, high-rate, hybrid electrical energy storage. *Acs Nano* **2011**, *5*, 8275-8287.
- (47) Toupin, M.; Brousse, T.; Bélanger, D. Charge storage mechanism of MnO2 electrode used in aqueous electrochemical capacitor. *Chemistry of Materials* **2004**, *16*, 3184-3190.
- (48) Poyraz, A. S.; Huang, J.; Wu, L.; Bock, D. C.; Zhu, Y.; Marschilok, A. C.; Takeuchi, K. J.; Takeuchi, E. S. Potassium-Based α-Manganese Dioxide Nanofiber Binder-Free Self-Supporting Electrodes: A Design Strategy for High Energy Density Batteries. *Energy Technology* **2016**, *4*, 1358-1368.

- (49) Kumagai, N.; Sasaki, T.; Oshitari, S.; Komaba, S. Characterization and lithium insertion characteristics of hollandite-type Ky (Mn 1– x M x) O 2 for rechargeable lithium battery electrodes. *J. New Mater. Electrochem. Syst* **2006**, *9*, 175-180.
- (50) Ling, C.; Mizuno, F. Capture Lithium in αMnO2: Insights from First Principles. *Chemistry of Materials* **2012**, *24*, 3943-3951.
- (51) Tompsett, D. A.; Islam, M. S. Electrochemistry of hollandite  $\alpha$ -MnO2: Li-ion and Na-ion insertion and Li2O incorporation. *Chemistry of Materials* **2013**, 25, 2515-2526.
- (52) Yuan, Y.; Nie, A.; Odegard, G. M.; Xu, R.; Zhou, D.; Santhanagopalan, S.; He, K.; Asayesh-Ardakani, H.; Meng, D. D.; Klie, R. F. Asynchronous Crystal Cell Expansion during Lithiation of K+-Stabilized α-MnO2. *Nano letters* **2015**, *15*, 2998-3007.



#### **Figures**

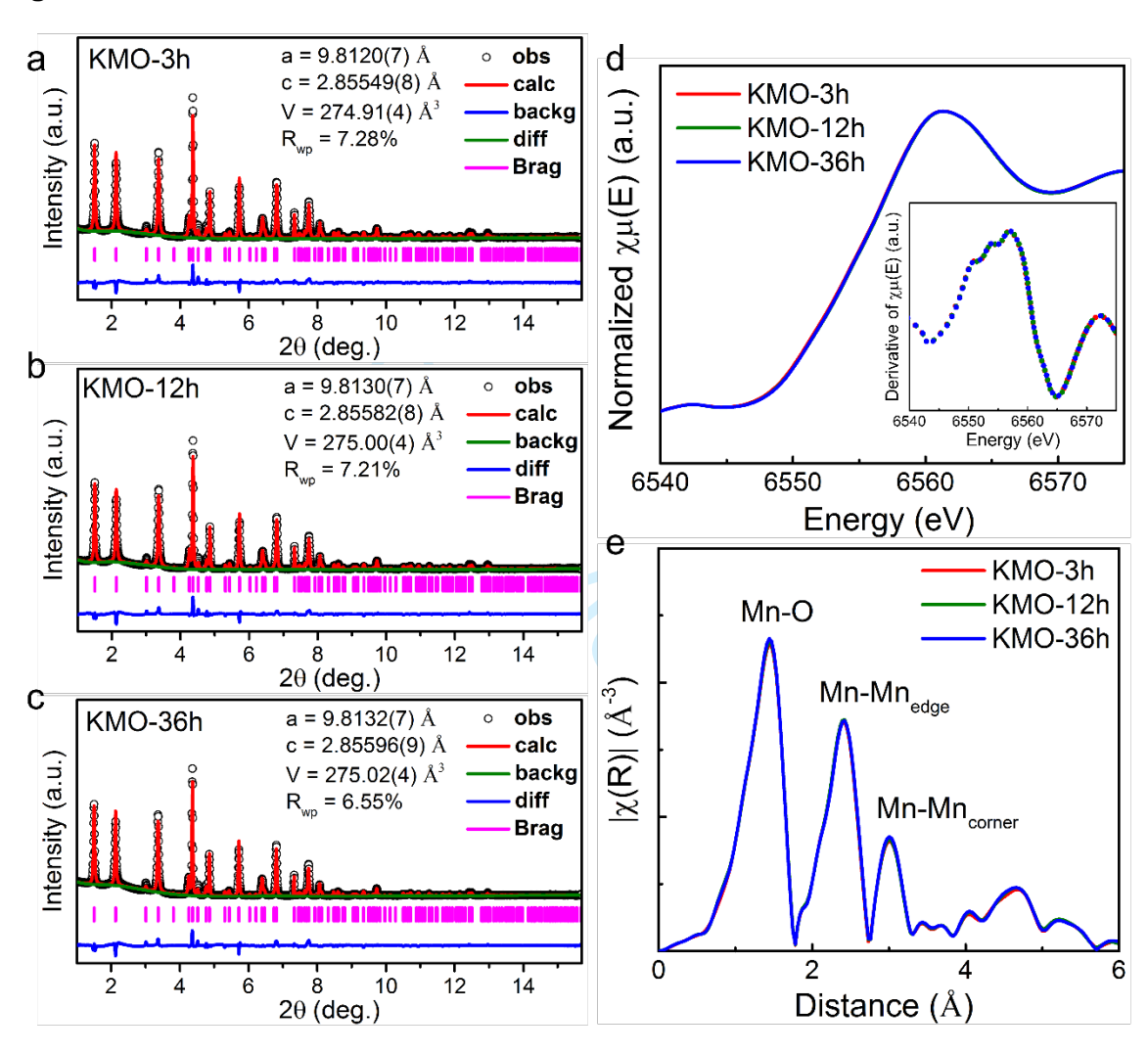


**Figure 1**. Rietveld refinement of synchrotron based XRD patterns for (a) KMO-3h, (b) KMO-12h, and (c) KMO-36h. Mn K-edge (d) XANES spectra with corresponding first derivative inset. (e) Fourier transformed EXAFS spectra for the KMO samples. Note: The Fourier transform is shown without phase correction, fitted bond distances are ~0.4 Å longer than radial distances depicted in the figure.

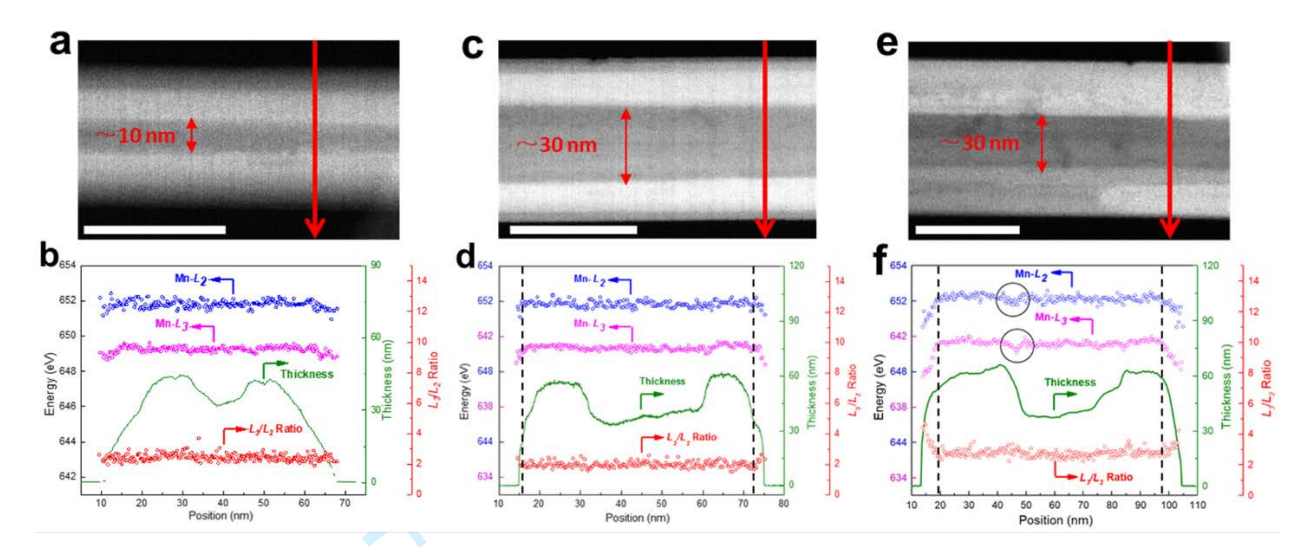


**Figure 2**. High magnification high-angle-annular-dark-filed (HAADF) images viewed along [100] zone-axis showing the representative microstructural features of the nanotube in (a) KMO-3h, (c) KMO-12h, and (e) KMO-36h sample. The scale bar in (a, c, e) is 50 nm. The arrows indicated the region used for spectrum imaging analyses. (b, d, f) detailed EELS analyses including the energy position of the Mn- $L_2$  edge, Mn- $L_3$  edge,  $L_3/L_2$  ratio and associated thickness variation along the corresponding red lines shown in (a, c, e). The dashed lines in (d, f) highlight the surface regions. The circles in (f) indicate the inner surfaces.

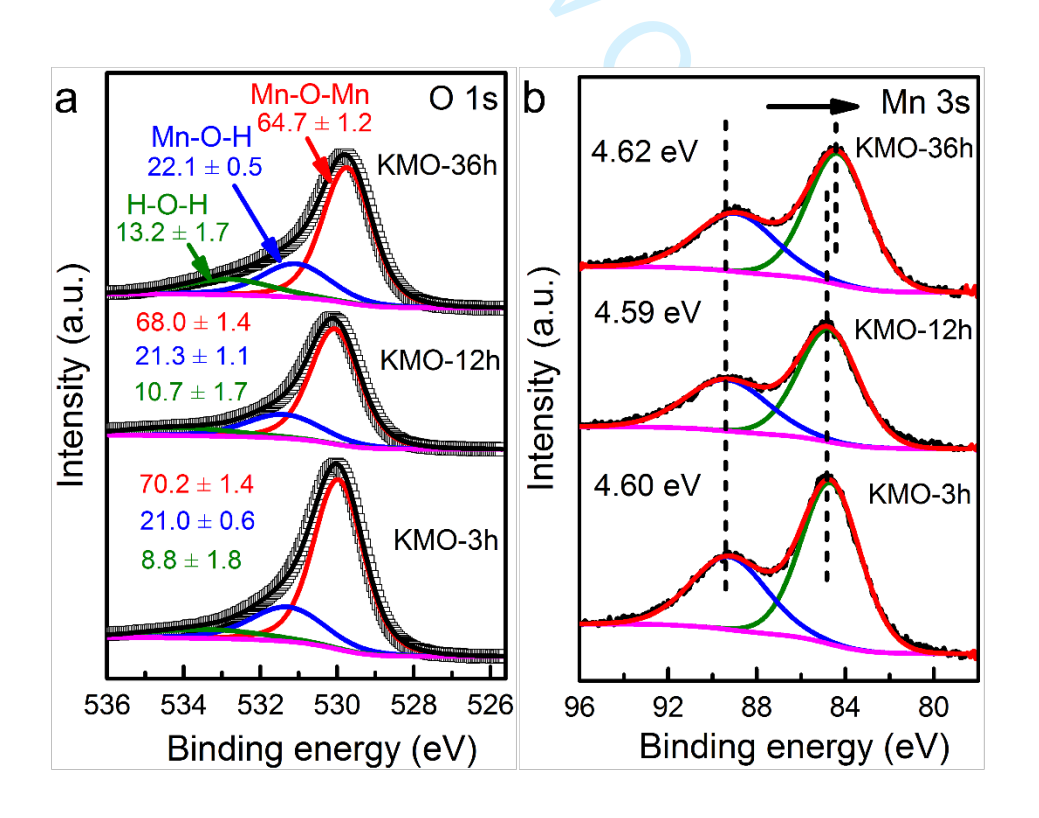


**Figure 3**. (a) O 1s and (b) Mn 3s regions of XPS spectra for KMO samples. O 1s spectra were fitted using three peaks representative of Mn-O-Mn (red), Mn-O-H (blue) and H-O-H (green) species, respectively. The fitted peak ratios are displayed in figure (a).

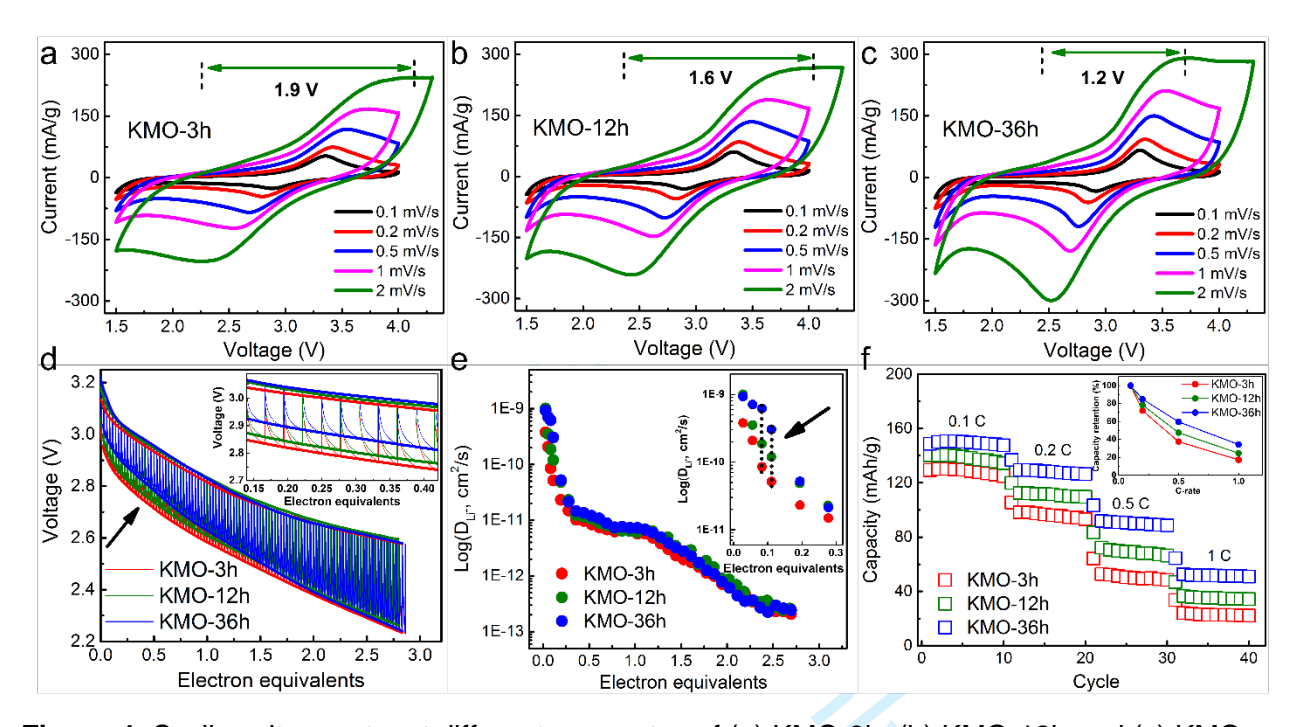


**Figure 4**. Cyclic voltammetry at different scan rates of (a) KMO-3h, (b) KMO-12h and (c) KMO-36h. (d) GITT type discharge profiles of the KMO samples. The inset shows the three samples have similar quasi-equilibrium open-circuit voltage while very different load voltages in the initial lithiation process. (e) Calculated Li ion diffusion coefficients of the KMO samples. The inset shows the Li ion diffusion coefficient of KMO-36h is ~1 order of magnitude higher than that of KMO-3h. (f) Rate capabilities of the KMO samples.

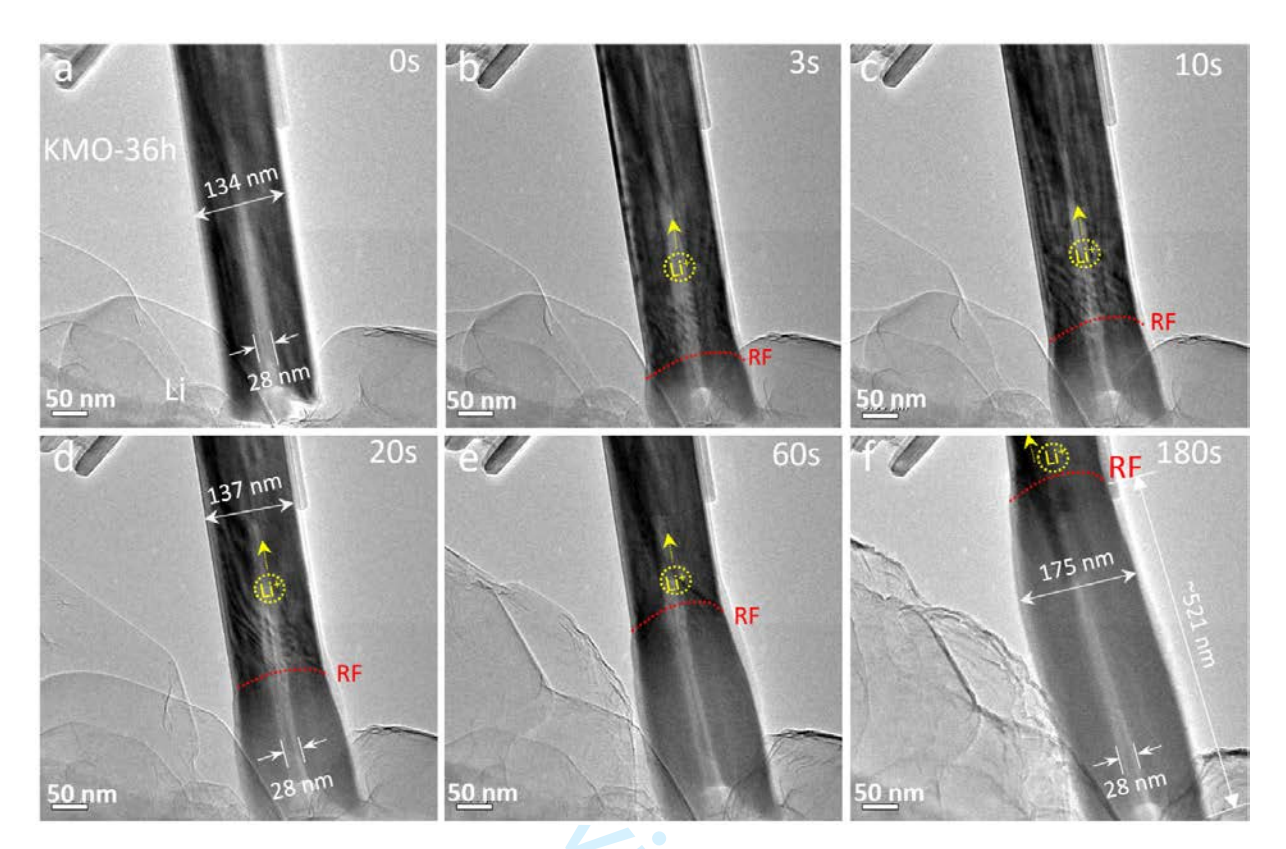


**Figure 5**. In situ TEM of the lithiation of a KMO-36h nanorod. (a-f) Propagation of the RF (marked in red) with considerable volume expansion of wall and no volume expansion of the hollow portion centrally located in the nanorod even at the fully lithiated region.

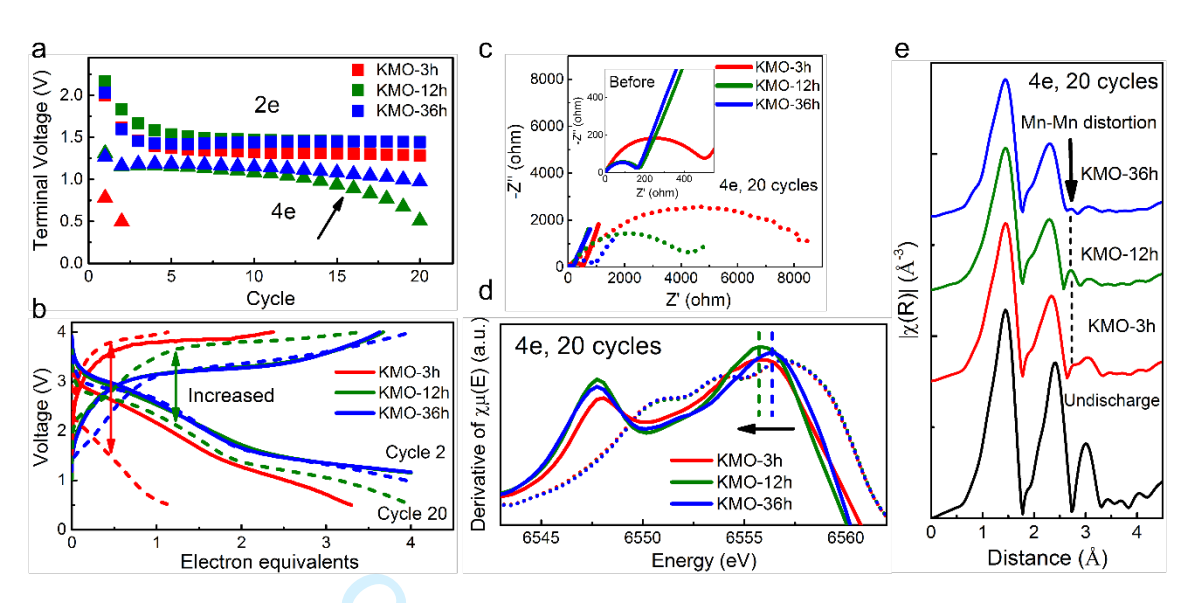


**Figure 6**. (a) Terminal voltages of KMO samples under 2 and 4 electron equivalents of reduction. (b) Discharge-charge profiles of KMO samples at cycle 2 (solid line) and cycle 20 (dashed line) under 4 electron equivalents of reduction. (c) Nyquist plots of the KMO samples before (solid line) and after (dashed line) 20 cycles under 4 e.e. reduction. (d) First derivative of Mn K-edge XANES spectra for the KMO samples before (dashed line) and after (solid line) 20 cycles under 4 e.e. reduction. (e) Mn K-edge EXAFS spectra for the KMO samples before and after 20 cycles.